processes

MDPI

Article

Mechanism and Modelling of Reactive Crystallization Process of Lithium Carbonate

Shaolei Zhao [1,†], Jie Gao [2,3,†], Siyang Ma [1], Chao Li [2,3], Yiming Ma [1], Yang He [1], Junbo Gong [1], Fu Zhou [4], Bingyuan Zhang [2,4] and Weiwei Tang [1,*]

1 School of Chemical Engineering and Technology, State Key Laboratory of Chemical Engineering, The Co-Innovation Center of Chemistry and Chemical Engineering of Tianjin, Tianjin University, Tianjin 300072, China; shaoleizhao@tju.edu.cn (S.Z.); siyang_ma@tju.edu.cn (S.M.); Marning_yimingma@126.com (Y.M.); yang_he@tju.edu.cn (Y.H.); junbo_gong@tju.edu.cn (J.G.)
2 Tianqi Lithium (Jiangsu) Co., Ltd., Zhang Jiagang 215634, China; jie.gao@tianqilithium.com (J.G.); lichao@tianqilithium.com (C.L.); zhangby@tianqilithium.com (B.Z.)
3 Tianqi Lithium Resources Recycling (Jiangsu) Co., Ltd., Zhang Jiagang 215600, China
4 Tianqi Lithium Corporation, Cheng Du 610000, China; zhoufu@tianqilithium.com
* Correspondence: wwtang@tju.edu.cn; Tel.: +86-22-2740-5754; Fax: +86-22-2737-4971
† The authors have contributed equally.

Received: 28 March 2019; Accepted: 23 April 2019; Published: 28 April 2019

Abstract: The reactive crystallization of lithium carbonate (Li_2CO_3) from lithium sulfate (Li_2SO_4) and sodium carbonate (Na_2CO_3) solutions is a key process in harvesting solid lithium, whether from ores, brines, or clays. However, the process kinetics and mechanism remain poorly understood and the modelling of the reactive crystallization of Li_2CO_3 is not available. Hence, this work aims to determine the kinetics and mechanisms of the nucleation and growth of Li_2CO_3 reactive crystallization by induction time measurements and to model and optimize the crystallization process using response surface methodology. Induction time measurements were carried out as functions of initial supersaturation and temperature using a laser method. It was found that the primary nucleation mechanism of Li_2CO_3 varies with solution supersaturations, in which, expectedly, the heterogenous nucleation mechanism dominates at low supersaturations while the homogeneous nucleation mode governs at high supersaturations. The transition point between heterogenous and homogenous nucleation was found to vary with temperatures. Growth modes of Li_2CO_3 crystals were investigated by relating induction time data with various growth mechanisms, revealing a two-dimensional nucleation-mediated growth mechanism. The modelling and optimization of a complex reactive crystallization were performed by response surface methodology (RSM), and the effects of various crystallization parameters on product and process performances were examined. Solution concentration was found to be the critical factor determining the yield of crystallization, while stirring speed was found to play a dominant role in the particle size of Li_2CO_3 crystals. Our findings may provide a better understanding of the reactive crystallization process of Li_2CO_3 and are critical in relation to the crystallization design and control of Li_2CO_3 production from lithium sulfate sources.

Keywords: lithium carbonate; reactive crystallization; crystallization mechanisms; multi-response optimization; response surface methodology

1. Introduction

Lithium and lithium compounds can be widely used due to their superior physical and chemical performance [1]. Among them, lithium carbonate (Li_2CO_3) is one important lithium compound used in

a wide range of applications such as rechargeable batteries, ceramics, glasses, and pharmaceuticals [2,3]. With the development of the lithium battery industry, the consumption of Li_2CO_3 will grow rapidly within the next few years, which will lead to a shortage of this resource in 2020 [4]. Therefore, it is necessary to develop sustained production of Li_2CO_3 to meet this increasing demand.

Nowadays, exploitation and processing of salt lake brines as well as lithium ores and lithium clays have been proven to be a feasible method of producing Li_2CO_3. Compared to the treatment of ores and clays, processing of brines is more economical and requires lower energy consumption [5]. However, there are currently few reports on the treatment of brines with high Mg/Li ratios, which increases the difficulty of recovering lithium resources from these matrices [6,7]. For this reason, the state-owned mining company Corporación Minera de Bolivia (COMIBOL) developed an alternative pilot process for the production of Li_2CO_3 from brines with a high Mg/Li ratio of 22:1 [5]. As can be seen from Figure 1, as one of the most critical steps in the production chain, the reactive crystallization of Li_2CO_3 from Li_2SO_4 and Na_2CO_3 solutions is the last carbonation stage of the pilot process. Furthermore, this reactive crystallization system for the production of Li_2CO_3 is also applied in other manufacturing processes using lithium-sulfated minerals such as lepidolite, spodumene, and amblygonite [8].

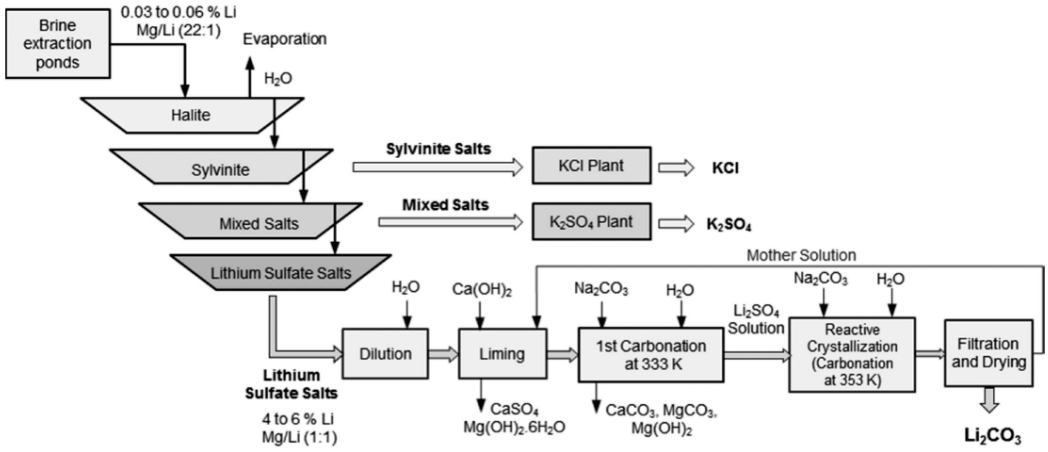

Figure 1. Flowsheet of the alternative pilot process used to produce Li_2CO_3 from brines with high Mg/Li ratios developed by COMIBOL. Reproduced with permission from Paola G. Aguilar and Teofilo A. Graber, Industrial and Engineering Chemistry Research; published by American Chemical Society, 2018.

Reactive crystallization of Li_2CO_3 plays a key role in recovering lithium resources, whether from ores, brines, or clays. Hence, this process has received significant interest. Sun et al. [9,10] measured the unseeded and seeded supersolubility data of Li_2CO_3 in aqueous solution using a laser apparatus and focused beam reflectance measurement (FBRM), respectively. By comparing the two methods, FBRM was found to be a better apparatus with which to detect nucleation events in the presence of seed. Wang et al. [11] measured the solubility, supersolubility, and metastable zone width of Li_2CO_3 in mixed lithium chloride (LiCl)-sodium chloride (NaCl)-potassium chloride (KCl)-sodium sulfate (Na_2SO_4) solutions at different temperatures and analyzed the effects of impurities on the thermodynamic properties of Li_2CO_3. Taborga et al. [12] have investigated the effects of different additives on the size and morphology of Li_2CO_3 crystals and have proposed that the presence of polyethylenimine (PEI), polyethylene glycol (PEG), and poly (4-styrenesulfonic acid) (P4SA) can increase the length of Li_2CO_3 crystals. Matsumoto et al. [13] developed a novel crystallization technique to produce Li_2CO_3 nanoparticles using minute gas-liquid interfaces around CO_2 microbubbles activated by microwave irradiation. The results showed that with the formation of numerous local supersaturation regions at the minute gas-liquid interfaces, fine-sized Li_2CO_3 particles with a narrow size distribution were crystallized due to the higher nucleation rate.

In the aforementioned studies, the thermodynamic properties of Li_2CO_3 and effects of different additives on its morphology were discussed and some novel methods for the production of Li_2CO_3

crystals were also reported [9–13]. However, there have been no works concentrating on the reactive crystallization mechanisms of Li_2CO_3 from Li_2SO_4 and Na_2CO_3 solutions and multi-objective optimization of the process. Here, the nucleation and growth kinetics and mechanisms of Li_2CO_3 in reactive crystallization are investigated and the complex reactive crystallization process is modeled and optimized using a novel method named response surface methodology. First, the induction times for the reactive crystallization of Li_2CO_3 were measured over a range of supersaturations at different temperatures using a laser method. Then, the effects of supersaturation levels and temperature on the nucleation behavior of Li_2CO_3 crystals were studied. Further, various mechanisms of crystal growth were examined and the crystal growth mode of Li_2CO_3 was determined on the basis of data fitting between experiments and theory. Finally, a response surface methodology (RSM) with central composite design (CCD) was developed to understand the effects of various operating parameters on the performance of the process. The significance of models was further revealed by analysis of variance (ANOVA).

2. Materials and Methods

2.1. Materials and Experimental Procedures

Lithium sulfate (99.9% metal basis) was purchased from Chemart Chemical Technology Co. Ltd. (Tianjin, China). Sodium carbonate (AR, ≥99.8%) was purchased from Titan Scientific Co. Ltd. (Shanghai, China). Water was filtered through a double-deionized purification system and was used as the solvent in all experiments. All chemicals were used directly without further purification.

The induction times were experimentally measured as functions of initial supersaturation and temperature using a laser method. In accordance with a previous work [9], a 100 mL crystallizer with a water bath (CF41, Julabo, Germany), a temperature indicator (Pt-100, Julabo, Germany), an overhead mechanical stirrer (WB-2000C, Julabo, Germany), and a laser apparatus (JSW3-300, Mettler Toledo, Switzerland) were used for induction time measurement. Firstly, a 40 mL Li_2SO_4 solution was introduced into the crystallizer and then agitation at 300 rpm in a water bath was initiated. When the solution temperature stabilized, the preheated 40 mL Na_2CO_3 solution was poured into the crystallizer and the laser apparatus was turned on simultaneously; this was recorded as the start time. The same molar concentration of Li_2SO_4 and Na_2CO_3 solution was calculated according to the specified supersaturation. In the initial period, the solution was clear and the light intensity stayed constant, whereas when the primary nucleation occurred, the light intensity decreased sharply due to the diffraction and dispersion effect. The induction time can be calculated according to the interval between the start time and the time when the light intensity decreases sharply. During the experiment, the crystallizer was sealed to avoid the occurrence of water evaporation.

The experimental set up for optimizing the reactive crystallization process is similar to the induction time measurement set up. Firstly, 40 mL Li_2SO_4 solution was introduced into the crystallizer, and then water-bath agitation was initiated. When the solution temperature stabilized, the peristaltic pump was turned on to feed the Na_2CO_3 solution. The molar concentration of the Li_2SO_4 and Na_2CO_3 solutions was the same. Upon finishing feeding, the crystallizer was sealed and the solution temperature was kept constant for 150 min to ensure that the Li_2CO_3 crystals grew sufficiently. After the reaction, the slurry was filtered while hot and the filter cake was washed three times with absolute ethanol and dried in an oven at 50 °C for 12 h to remove free water. Finally, the particle size and crystal size distribution of the Li_2CO_3 product were analyzed using Morphology 3000 (Malvern, UK).

2.2. Theory

2.2.1. Classical Nucleation Theory

According to classical nucleation theory [14], the nucleation rate (J) can be expressed according to Equation (1), i.e.,

$$\mathrm{J} = A\exp\left(-\frac{\beta{\gamma_{\mathrm{sl}}}^3 v^2}{(k_B T)^3 (lnS)^2}\right) \tag{1}$$

where A is the pre-exponential factor, β is the geometric factor, γ_{sl} is the interfacial free energy, v is the molecular volume, k_B is the Boltzmann constant, T is the absolute temperature, and S is the supersaturation.

Generally, the induction time $\mathrm{t_{ind}}$ consists of three parts: the relaxation time, $\mathrm{t_r}$; the time required to generate a stable nucleus, $\mathrm{t_n}$; and the time required for the nucleus to grow to be detectable, $\mathrm{t_g}$. Making the assumption that the $\mathrm{t_{ind}}$ is mainly composed of $\mathrm{t_n}$, which is inversely proportional to the nucleation rate, we get:

$$\mathrm{J} = \mathrm{K}\cdot {t_{ind}}^{-1} \tag{2}$$

Combining Equations (1) and (2), the relationship between induction time and supersaturation can be given by:

$$t_{ind} = \frac{K}{A}\exp\left[\frac{\beta{\gamma_{\mathrm{sl}}}^3 v^2}{(k_B T)^3 (lnS)^2}\right] \tag{3}$$

Taking the logarithm of both sides of Equation (3) and rearranging gives:

$$\ln t_{ind} = \frac{\beta{\gamma_{\mathrm{sl}}}^3 v^2}{(k_B T)^3 (lnS)^2} + \mathrm{B} \tag{4}$$

Equation (4) has been proved to be valid by Sohnel and Mullin when the induction time is mainly dominated by the time required to generate a stable nucleus [15].

Supersaturation is an important factor affecting the nucleation rate. In addition to classical nucleation theory, the nucleation rate can also be considered a function of supersaturation, as shown in the following empirical equation, Equation (5). The effect of supersaturation on the nucleation rate can be visually reflected by determining the nucleation order. The empirical equation can be given by:

$$\mathrm{J} = k\Delta C^n \tag{5}$$

Combining Equations (2) and (5), we get:

$$t_{ind} = \frac{K}{k(\Delta \mathrm{C})^n} \tag{6}$$

The relationship between relative supersaturation and the supersaturation ratio can be expressed as:

$$\sigma = \mathrm{S} - 1 = \frac{\Delta C}{C^*} \tag{7}$$

Combining Equations (6) and (7), the relationship between induction time and relative supersaturation can be given by:

$$t_{ind} = \frac{K}{k(\sigma \mathrm{C}^*)^n} \tag{8}$$

Taking the logarithm of both sides of Equation (8) and rearranging gives:

$$\ln t_{ind} = \ln\left[\frac{K}{k(C^*)^n}\right] - nln(\sigma) \tag{9}$$

Equation (9) reveals that there is a linear relationship between $\ln t_{ind}$ and $ln(\sigma)$, which can be employed to determine the nucleation order n at a given temperature.

2.2.2. Mechanism of Crystal Growth

The growth mode of the Li_2CO_3 crystal was identified by fitting the induction time data measured from reactive crystallization experiments over a range of supersaturations at different temperatures using expressions derived by Van der Leeden et al. [16], which can be expressed by

$$t_{ind} = \frac{1}{JV} + \left[\frac{\alpha}{a_n J G^{n-1}}\right]^{\frac{1}{n}} \tag{10}$$

where J is the nucleation rate, V is the volume of the system, α is the volume fraction of the new phase formed, a_n is a shape factor, G is the growth rate, and n = mv + 1 (m is the dimensionality of growth and $0.5 < \nu < 1$). As for Equation (10), the first term which originates from the mononuclear mechanism is often negligible in comparison to the second term because of the polynuclear mechanism. For three-dimensional nucleation, the steady-state nucleation rate can be given as

$$\mathrm{J} = K_J S exp\left(-\frac{B}{ln^2 S}\right) \tag{11}$$

where K_J is the nucleation rate constant and $B = \frac{\beta {\gamma_{sl}}^3 v^2}{(k_B T)^3}$.

The relationship between the growth rate and supersaturation is generally described as

$$\mathrm{G} = K_G f(\mathrm{S}) \tag{12}$$

in which K_G is the growth rate constant and $f(\mathrm{S})$ is a function of supersaturation depending on the growth mechanism. The expressions of $f(\mathrm{S})$ corresponding to different growth mechanisms are shown in Table 1.

Table 1. The expressions of $f(\mathrm{S})$ for different growth mechanisms.

	Growth Mechanisms	***f*(S)**
F_1	Normal growth	$(S-1)$
F_2	Spiral growth	$(S-1)^2$
F_3	Volume diffusion-controlled growth	$(S-1)$
F_4	2D nucleation-mediated growth	$(S-1)^{\frac{2}{3}} S^{\frac{1}{3}} \exp\left(\frac{-B_{2D}}{3lnS}\right)$

Combining Equations (10)–(12), we get

$$t_{ind} = A_u [f(S)]^{(\frac{1}{n}-1)} S^{-\frac{1}{n}} \exp\left(\frac{B}{nln^2 S}\right) \tag{13}$$

where

$$A_u = \left(\frac{\alpha}{a_n K_J {K_G}^{n-1}}\right)^{\frac{1}{n}} \tag{14}$$

For normal, spiral, and volume diffusion-controlled growth, Equation (13) can be rearranged to give

$$F_u(\mathrm{S}) = \ln A_u + \frac{B}{nln^2 S} \tag{15}$$

where

$$F_u(\mathrm{S}) = \ln\left\{t_{ind}[f(S)]^{\frac{n-1}{n}} S^{\frac{1}{n}}\right\} \tag{16}$$

Hence, as can be seen from Equation (15), a plot of $F_u(\mathrm{S})$ versus $1/(\ln^2 \mathrm{S})$ can be fitted using a straight line for different values of n.

For 2D nucleation-mediated growth, Equation (13) can be rearranged to give

$$F_u(\mathrm{S}) = \ln A_u + (n-1)\frac{B_{2D}}{3n \ln S} + \frac{B}{n ln^2 S} \tag{17}$$

where

$$F_u(\mathrm{S}) = \ln\left\{t_{ind}(\mathrm{S}-1)^{\frac{2(n-1)}{3n}} S^{\frac{n+2}{3n}}\right\} \tag{18}$$

In this case, a plot of $F_u(\mathrm{S})$ versus $1/(\ln \mathrm{S})$ can be fitted using a parabolic model for different values of n. Depending on the goodness of fit, the growth mechanism can be identified as being either normal, spiral, or volume diffusion-controlled, or 2D nucleation-mediated, growth.

2.3. Response Surface Methodology and ANOVA Modeling

RSM combined with CCD is an efficient method with which to explore the relationships between operating factors and system responses [17], and is widely used in process design and optimization [18]. The design procedure for RSM can be summarized as follows [17]: design a series of experiments to achieve sufficient and reliable measurement for the desired response; develop a mathematical model with a polynomial form and maximum fitting; analyze the direct and interactive effects of operating parameters on responses from the plotted response surface; determine the optimal experimental parameters in order to produce the most desirable value of the response.

Central composite design requires three types of tests: 2^k factorial tests, 2k axial tests, and n_c center point tests, where k is the number of factors investigated in the experiment [19]. The design is represented by five levels: $-\alpha$, -1, 0, 1, and α, where α is equal to $(2^k)^{0.25}$ [20]. The experimental data is used to develop a mathematical model with a polynomial form. The significance of each term in the equation and the goodness of fitting quality can be validated by ANOVA. Response surfaces were plotted based on the fitted polynomial model.

Crystallization temperature (°C), feeding rate (mL/min), concentration (mol/L), and stirring speed (rpm) were considered as factors in this research. The yield (%) and particle size (μm) of Li_2CO_3 product were considered as responses. A CCD design with four factors at five levels with 30 simulations test was developed in this work. Design Expert 8.0.6 trial version (Stat-Ease, Inc., Minneapolis, MN, USA) was used for this analysis.

3. Results and Discussion

3.1. Kinetics and Mechanism of Li_2CO_3 Reactive Crystallization

3.1.1. Induction Time Measurements

The experimentally measured induction times are significant in the process design and control of an efficient crystallization system. For example, in antisolvent crystallization, if the mixing time of the solvent and antisolvent can be controlled in a period shorter than the induction time, fine-sized particles of narrow size distributions may be achieved [21]. In addition, analysis of the induction time based on nucleation and growth theory also help in understanding the mechanisms of nucleation and growth [14]. Therefore, a laser apparatus was used to provide a reliable method for the measurement of induction times in this work, and the results are shown in Figure 2.

Generally, the relationship between induction time (t_{ind}) and supersaturation (S) can be correlated using the following empirical equation:

$$t_{ind} = \frac{A_{ind}}{S^r} \tag{19}$$

where A_{ind} and r are empirical constants [22]. The induction times measured at different temperatures were correlated with the supersaturation and the values of the empirical constants A_{ind} and r were obtained and are shown in Table 2.

Table 2. The parameters of empirical Equation (19) at different temperatures.

T (K)	A_{ind}	r	R^2
318.15	5.2844×10^5	6.0625	0.9969
323.15	7.8263×10^5	7.2975	0.9919
328.15	4.8841×10^5	7.5533	0.9901
333.15	2.5222×10^5	7.5568	0.9913

As can be seen from Figure 2 and Table 2, the induction time and supersaturation can be well correlated at different temperatures by Equation (19), and all the coefficients of determination, R^2, are above 0.99. Meanwhile, it can be seen that at the same temperature, with the level of supersaturation increasing, the induction time is shortened. This is because when a higher supersaturation level is created, the nucleation driving force is larger and thus the nucleation rate is improved, which as a result shortens the nucleation induction time. Similarly, at the same supersaturation level, the induction time will be significantly shortened with increasing temperature. This is because the movement of ions can be accelerated at higher temperatures which increases the collision frequency of ions, thus promoting the formation of crystal nuclei. This phenomenon is consistent with classical nucleation theory.

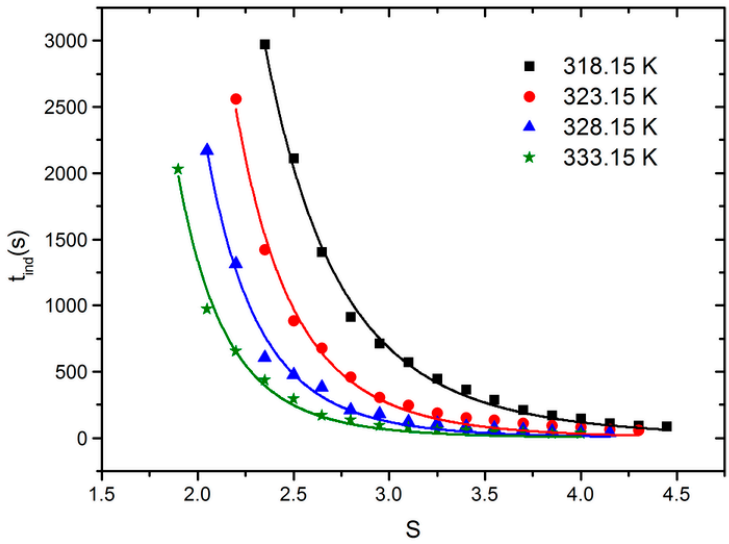

Figure 2. The nucleation induction times of Li_2CO_3 at different temperatures and supersaturations.

3.1.2. Crystal Nucleation Kinetics and Mechanism

For the primary nucleation process, the relationship between induction time and supersaturation can be expressed by Equation (4). In order to have a better understanding of the nucleation behavior of Li_2CO_3 under different conditions, $\log(t_{ind})$ was plotted versus $(\log S)^{-2}$, with the result shown in Figure 3. As can be seen from Figure 3, the experimental data follows the linear relationship given by Equation (4). However, there is a region of higher slope at higher supersaturation and a region of lower slope at lower supersaturation. Similar results have been reported for inorganic salts by other researchers [23,24]. This phenomenon can be attributed to a change in nucleation mechanism. At lower supersaturation levels, the driving force of the phase transition is lower and the nucleation process is easily affected by external particles, so the heterogeneous nucleation mechanism plays a leading role in the nucleation process. At higher supersaturation levels, the driving force of phase transition is larger. Compared with the spontaneous nucleation of solution, the influence of external particles on

the nucleation process can be neglected, and thus the homogeneous nucleation mechanism dominates the nucleation process.

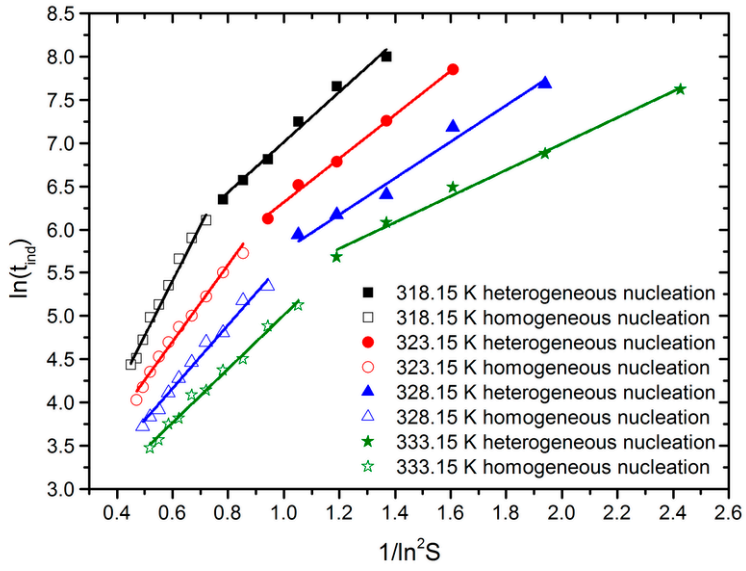

Figure 3. Plot of $\log(t_{ind})$ versus $(\log S)^{-2}$ for Li_2CO_3 crystallization.

Mersmann et al. [25] have proposed that for the reactive crystallization of insoluble materials, the transition supersaturation (S_t) required for homogeneous nucleation should be greater than 2. For the reactive crystallization of Li_2CO_3 in our study, the transition supersaturation (S_t) is not a fixed value. As can be seen from Figure 3, from 318.15 K to 333.15 K, the transition supersaturation (S_t) is 3.23, 2.85, 2.62, and 2.41, respectively.

According to Equation (9), the nucleation order n can be obtained by fitting $\ln t_{ind}$ and $ln(\sigma)$ using a linear function, with the result shown in Figure 4. As can be seen from Figure 4, the test points show a good linear relationship as a whole, and the regression curves are almost parallel to each other under different temperatures, indicating that the nucleation order is similar under the experimental conditions used. From 318.15 K to 333.15 K, the nucleation order is 3.84, 3.68, 3.60, and 3.48, respectively.

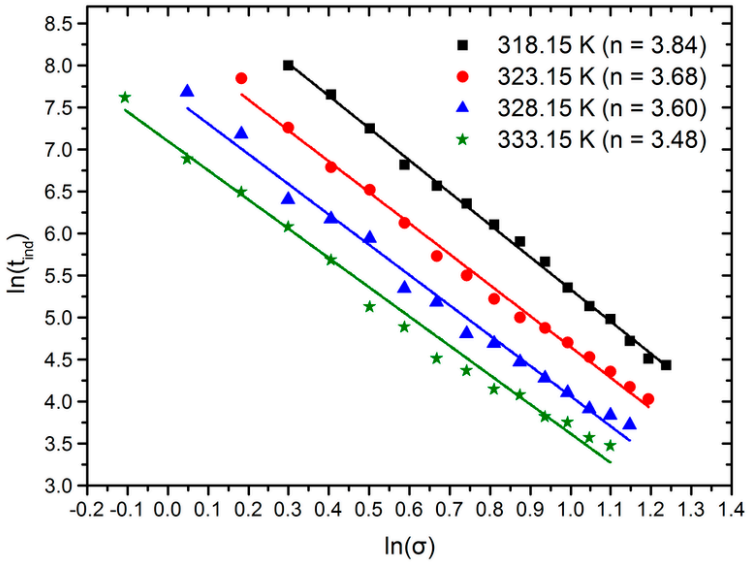

Figure 4. Plot of $\log(t_{ind})$ versus $ln(\sigma)$ for Li_2CO_3 crystallization.

3.1.3. Identification of Crystal Growth Mechanism

The growth-mechanism of Li_2CO_3 crystals was identified by fitting the experimental induction times from reactive crystallization over a range of temperatures and supersaturations to the expressions of different growth mechanisms. According to a previous study [26], Li_2CO_3 crystals are rod-like, meaning the value of m is 1. Hence n (mν + 1) can take values of either 3/2 or 2 depending on the value of ν (1/2 or 1). The expressions $F_u(S)$ for different growth mechanisms of Li_2CO_3 are shown in Table 3.

Table 3. The expressions $F_u(S)$ for different growth mechanisms of Li_2CO_3.

	Growth Mechanisms	ν	n	$F_u(S)$
F_1	Normal growth	1	2	$\ln\left\{t_{ind}(S-1)^{\frac{1}{2}}S^{\frac{1}{2}}\right\}$
F_2	Spiral growth	1	2	$\ln\left\{t_{ind}(S-1)S^{\frac{1}{2}}\right\}$
F_3	Volume diffusion-controlled growth	1/2	3/2	$\ln\left\{t_{ind}(S-1)^{\frac{1}{3}}S^{\frac{2}{3}}\right\}$.
F_4	2D nucleation-mediated growth	1	2	$\ln\left\{t_{ind}(S-1)^{\frac{1}{3}}S^{\frac{2}{3}}\right\}$

For mechanisms F_1, F_2, and F_3, $F_u(S)$ and $1/ln^2S$ are in a linear relationship, while for mechanism F_4, $F_u(S)$ and $1/\ln S$ are in a quadratic polynomial relationship. The calculated values of $F_u(S)$ were plotted against either $1/\ln S$ or $1/ln^2S$, with the results shown in Figure 5. Depending on the goodness of fitting quality shown in Table 4, the growth mechanism can be identified.

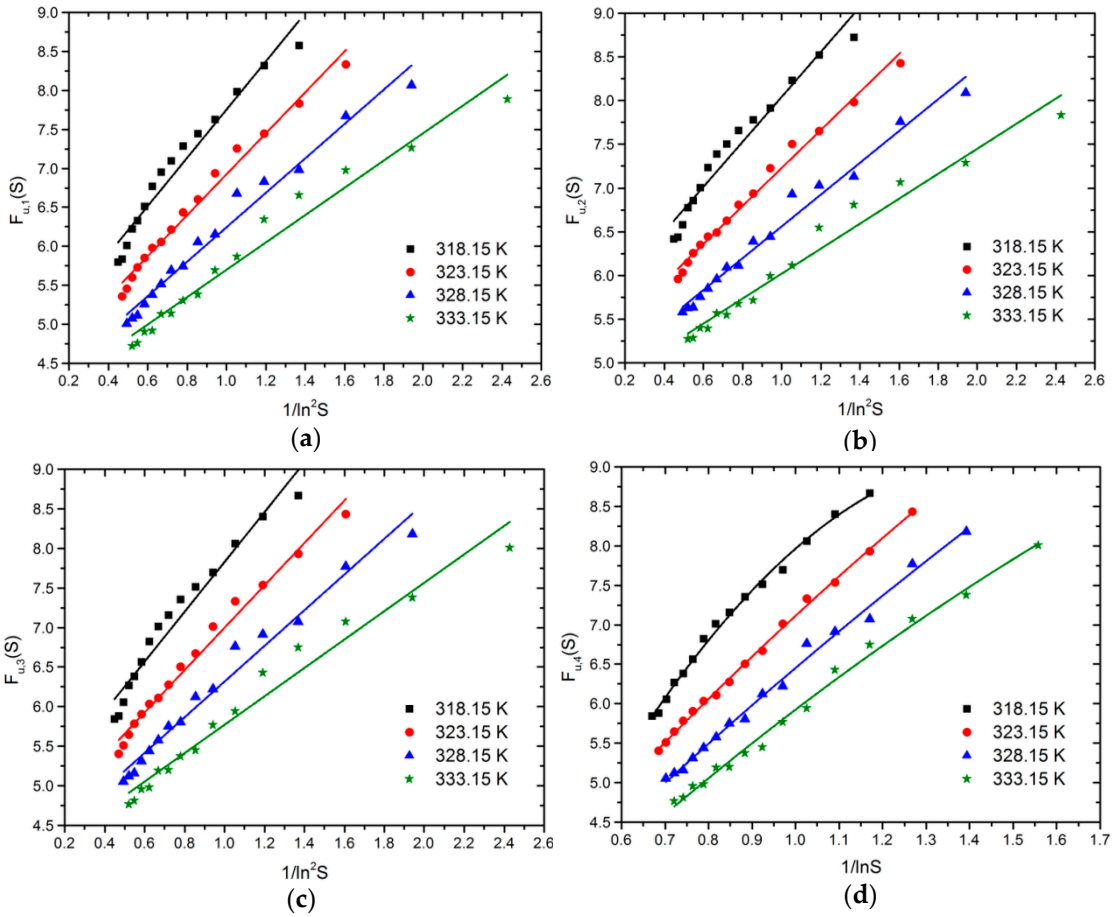

Figure 5. Plot of $F_u(S)$ versus $1/\ln S$ or $1/ln^2S$ for Li_2CO_3 crystals. Data are fitted using (**a**) normal growth, (**b**) spiral growth, (**c**) volume diffusion-controlled growth, and (**d**) 2D nucleation-mediated growth.

Table 4. The coefficients of determination R^2 for different growth mechanisms of Li_2CO_3 under different temperatures.

T (K)	R^2			
	F_1	F_2	F_3	F_4
318.15	0.9530	0.9505	0.9539	0.9949
323.15	0.9843	0.9877	0.9843	0.9977
328.15	0.9768	0.9785	0.9771	0.9918
333.15	0.9674	0.9699	0.9677	0.9920
Ave.R^2	0.9704	0.9717	0.9708	0.9941

It can be seen from Figure 5 and Table 4 that the F_4 mechanism correlates the induction time and supersaturation data well at different temperatures using a quadratic polynomial. The coefficients of determination R^2 are above 0.99 and the fitting accuracy is high. Hence, it can be concluded that the growth mode of Li_2CO_3 crystals under our experimental conditions is a 2D nucleation-mediated growth mechanism.

3.2. Multi-response Optimization Using Response Surface Methodology

3.2.1. Central Composite Design and Crystallization Outcomes

Based on single factor tests, a CCD of an RSM was employed to investigate the effects of four variables—temperature (A), feeding rate (B), concentration (C), and stirring speed (D)—on the yield (Y_1) and particle size (Y_2) of the Li_2CO_3 product. The experimental factors were coded at five levels (−2, −1, 0, 1, 2), and temperature (30, 40, 50, 60, 70 °C), feeding rate (1, 2, 3, 4, 5 mL/min), concentration (1.5, 1.75, 2, 2.25, 2.5 mol/L) and stirring speed (200, 300, 400, 500, 600 rpm) were investigated (Table 5). This design was composed of 30 tested points, including six replications of the zero points. The response results are shown in Table 6.

Table 5. Levels and codes of central composite design.

Level	Factor			
	Temperature °C	Feeding Rate mL/min	Concentration mol/L	Stirring Speed rpm
−2	30	1	1.5	200
−1	40	2	1.75	300
0	50	3	2	400
1	60	4	2.25	500
2	70	5	2.5	600

Table 6. Central composite design and experimental results.

Run	Temperature °C	Feeding Rate mL/min	Concentration mol/L	Stirring Speed rpm	Yield %	D [4,3] µm
1	40.00	4.00	1.75	500.00	71.50	107.00
2	50.00	3.00	2.00	400.00	88.59	101.00
3	60.00	2.00	1.75	300.00	77.78	138.00
4	40.00	2.00	2.25	500.00	83.72	94.50
5	30.00	3.00	2.00	400.00	73.54	109.00
6	40.00	4.00	2.25	300.00	88.24	108.00
7	70.00	3.00	2.00	400.00	88.46	82.00
8	50.00	3.00	2.00	200.00	86.31	180.00
9	50.00	3.00	1.50	400.00	79.52	130.00
10	60.00	4.00	2.25	300.00	89.89	126.00

Table 6. *Cont.*

Run	Temperature °C	Feeding Rate mL/min	Concentration mol/L	Stirring Speed rpm	Yield %	D [4,3] µm
11	40.00	2.00	1.75	300.00	71.43	140.00
12	60.00	4.00	2.25	500.00	90.91	90.70
13	60.00	4.00	1.75	300.00	78.35	135.00
14	50.00	3.00	2.50	400.00	83.05	90.60
15	50.00	3.00	2.00	400.00	88.03	108.00
16	60.00	2.00	2.25	300.00	80.36	134.00
17	60.00	2.00	1.75	500.00	79.15	110.00
18	50.00	3.00	2.00	400.00	87.73	101.00
19	60.00	2.00	2.25	500.00	80.71	104.00
20	50.00	3.00	2.00	400.00	90.42	93.10
21	40.00	4.00	1.75	300.00	72.91	131.00
22	40.00	4.00	2.25	500.00	87.83	92.50
23	40.00	2.00	1.75	500.00	72.07	109.00
24	50.00	5.00	2.00	400.00	87.54	92.60
25	50.00	1.00	2.00	400.00	86.87	98.70
26	50.00	3.00	2.00	400.00	88.46	96.80
27	60.00	4.00	1.75	500.00	78.70	113.00
28	40.00	2.00	2.25	300.00	85.50	122.00
29	50.00	3.00	2.00	400.00	89.71	96.20
30	50.00	3.00	2.00	600.00	87.36	91.50

3.2.2. Model Fitting and ANOVA Analysis

The experimental data was used to develop a second-order polynomial model which can be written as:

$$Y = \beta_0 + \sum_{i=1}^{k} \beta_i \times A_i + \sum_{i=1}^{k} \sum_{j=1}^{k} \beta_{ij} \times A_i \times A_j + \sum_{i=1}^{k} \beta_{ii} \times {A_i}^2 + \varepsilon \quad (20)$$

in which β_0 is the intercept, β_i, β_{ij}, β_{ii} are first-order, interactive, and second-order effects, respectively, i and j represent the number of k factors, and ε is the residual error [27]. This method is able to evaluate interaction effects and pure quadratic effects, and is considered to be the most efficient evaluation method that can improve the quality of data.

ANOVA was used to determine the significance of each term in the equation and estimate the goodness of fitting quality. In the results of this ANOVA analysis the p-values could be used to check the significance of each term. Specifically, values of "probability (p) > F" less than 0.05, 0.01, and 0.001 indicate that the model terms are significant, highly significant, and remarkably significant, respectively, while values greater than 0.05 indicate that the model terms are not significant [28].

The results of ANOVA for the quadratic model of the yield are shown in Table 7. ANOVA revealed that the model was highly significant ($p < 0.01$) for the yield of Li_2CO_3 product, indicating that the developed model was reliable. As can be seen from Table 7, significant linear A, highly significant quadratic A^2 and C^2, and remarkably significant linear C effects on yield were shown by the ANOVA results, while for the other factors, the p-values were greater than 0.05, indicating that these factors were not significant. Based on the regression coefficient (β) values, solution concentration was revealed to be a major effect, followed by temperature, feeding rate, and stirring speed. The yield of the Li_2CO_3 product can be expressed by the following second order polynomial equation:

$$\begin{aligned} R(\text{Yield}) = {} & 88.82 + 2.19^{a} + 1.21B + 3.85C + 0.092D + 0.76AB - 1.84AC + 0.38AD + 1.60BC - \\ & 0.064BD - 0.11CD - 2.54A^2 - 0.99B^2 - 2.47C^2 - 1.08D^2 \end{aligned} \quad (21)$$

Table 7. ANOVA analysis and results with quadratic model of yield.

Source	Sum of Squares	Degrees of Freedom	Mean Square	F-Value	*p*-Value
Model	922.17	14	65.87	4.26	0.0043
A–Temperature	114.84	1	114.84	7.42	0.0157
B–Feeding Rate	34.90	1	34.90	2.25	0.1540
C–Concentration	355.17	1	355.17	22.95	0.0002
D–Stirring speed	0.20	1	0.20	0.01	0.9103
AB	9.13	1	9.13	0.59	0.4544
AC	54.36	1	54.36	3.51	0.0805
AD	2.28	1	2.28	0.15	0.7063
BC	40.88	1	40.88	2.64	0.1249
BD	0.07	1	0.07	0.00	0.9487
CD	0.20	1	0.20	0.01	0.9100
A^2	177.08	1	177.08	11.44	0.0041
B^2	26.89	1	26.89	1.74	0.2073
C^2	167.32	1	167.32	10.81	0.0050
D^2	32.18	1	32.18	2.08	0.1699

Table 8 shows the ANOVA results using the quadratic model of particle size. ANOVA revealed that the model was remarkably significant ($p < 0.001$) for particle size for the Li_2CO_3 product, indicating that the developed model was very reliable. As shown in Table 8, linear C exhibited a highly significant effect on particle size and the linear D and quadratic D^2 displayed a remarkably significant effect, while for the other factors, the *p*-values are greater than 0.05, suggesting that these factors are not significant. Among the factors, particle size depended more on stirring speed, followed by concentration, feeding rate, and temperature. The fitted second order polynomial equation of particle size can be expressed as:

$$R(D\ [4,3]) = 99.35 - 0.30^{a} - 2.52B - 7.92C - 16.26D + 0.36AB + 1.79AC - 1.08AD - 1.64BC + 1.23BD - 0.21CD + 0.14A^2 + 0.18\ B^2 + 3.84C^2 + 10.20D^2 \quad (22)$$

Table 8. ANOVA analysis and results with quadratic model of particle size.

Source	Sum of Squares	Degrees of Freedom	Mean Square	F-Value	*p*-Value
Model	11293.00	14	806.64	8.40	< 0.0001
A–Temperature	2.22	1	2.22	0.02	0.8812
B–Feeding Rate	152.51	1	152.51	1.59	0.2268
C–Concentration	1505.75	1	1505.75	15.68	0.0013
D–Stirring speed	6347.25	1	6347.25	66.11	< 0.0001
AB	2.03	1	2.03	0.02	0.8863
AC	51.48	1	51.48	0.54	0.4753
AD	18.71	1	18.71	0.19	0.6652
BC	43.23	1	43.23	0.45	0.5124
BD	24.26	1	24.26	0.25	0.6225
CD	0.68	1	0.68	0.01	0.9340
A^2	0.54	1	0.54	0.01	0.9411
B^2	0.87	1	0.87	0.01	0.9254
C^2	404.58	1	404.58	4.21	0.0580
D^2	2855.42	1	2855.42	29.74	< 0.0001

3.2.3. Response Surface Analysis

Based on the equations mentioned above, three-dimensional surface values were depicted to show the influences of the independent variables (temperature, feeding rate, concentration, and stirring speed) on the yield and particle size of Li_2CO_3 product. The results are shown in Figures 6 and 7.

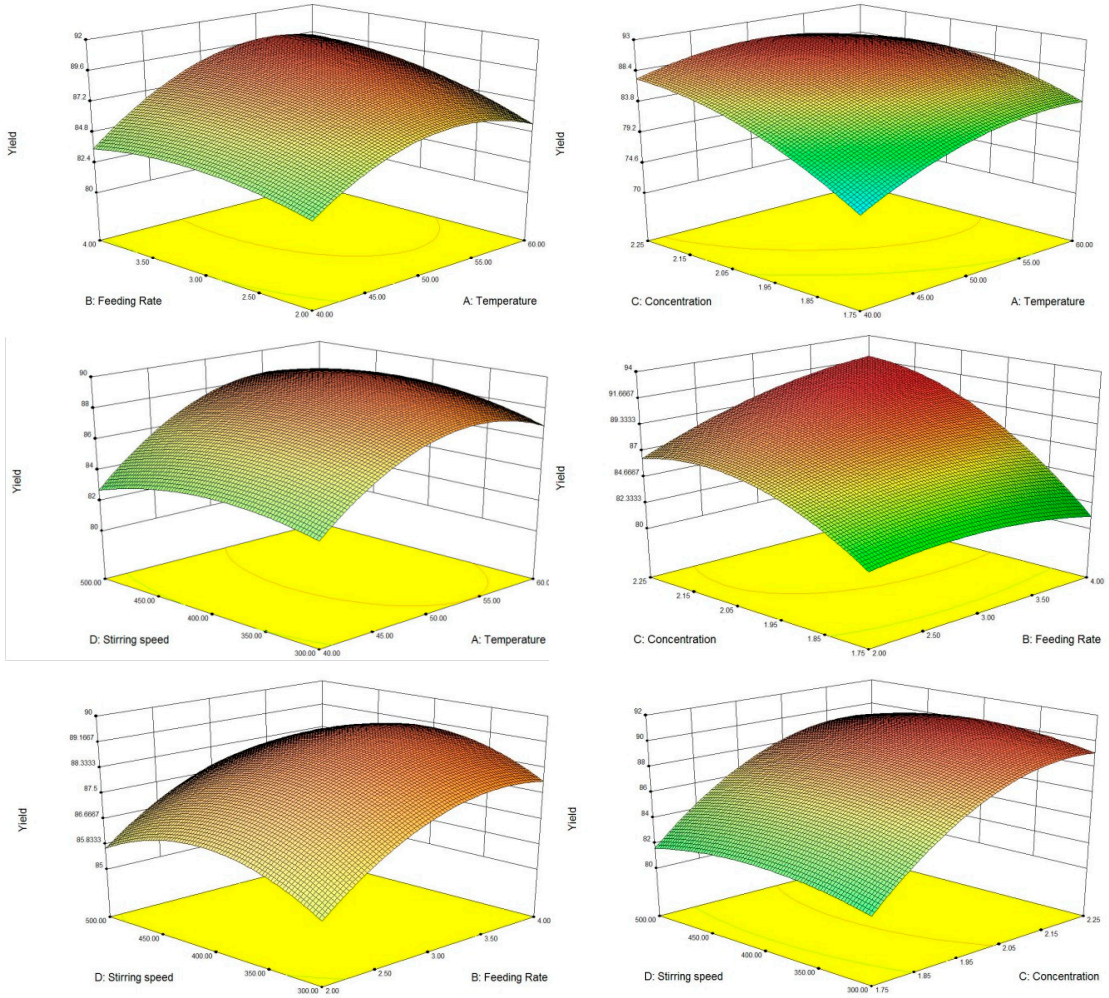

Figure 6. 3D surface plots of effects of binary interactions among factors A (temperature), B (feeding rate), C (concentration), and D (stirring speed) on response value Y_1 (yield of Li_2CO_3).

It can be seen from Figure 6 that the major factor affecting the yield of Li_2CO_3 was concentration of solution, and that interaction between various factors was not significant. Figure 6 also reveals that the yield of Li_2CO_3 increased with increasing concentration of solution. This is because increasing concentration improves instantaneous supersaturation, thus promoting the driving force of the nucleation and growth process. Therefore, more Li_2CO_3 could be crystallized in the same time, and the yield was improved.

As can be seen from Figure 7, the major factor affecting the particle size of Li_2CO_3 is stirring speed; the interaction between various factors is not significant. Figure 7 also reveals that the particle size of Li_2CO_3 decreased significantly with increasing stirring speed. This is because the improvement of stirring speed promotes ideal mixing conditions and thus the spatial distribution of the supersaturation becomes more uniform. Therefore, the supersaturation was mainly consumed by nucleation and the growth process was suppressed, meaning that the particle size was reduced.

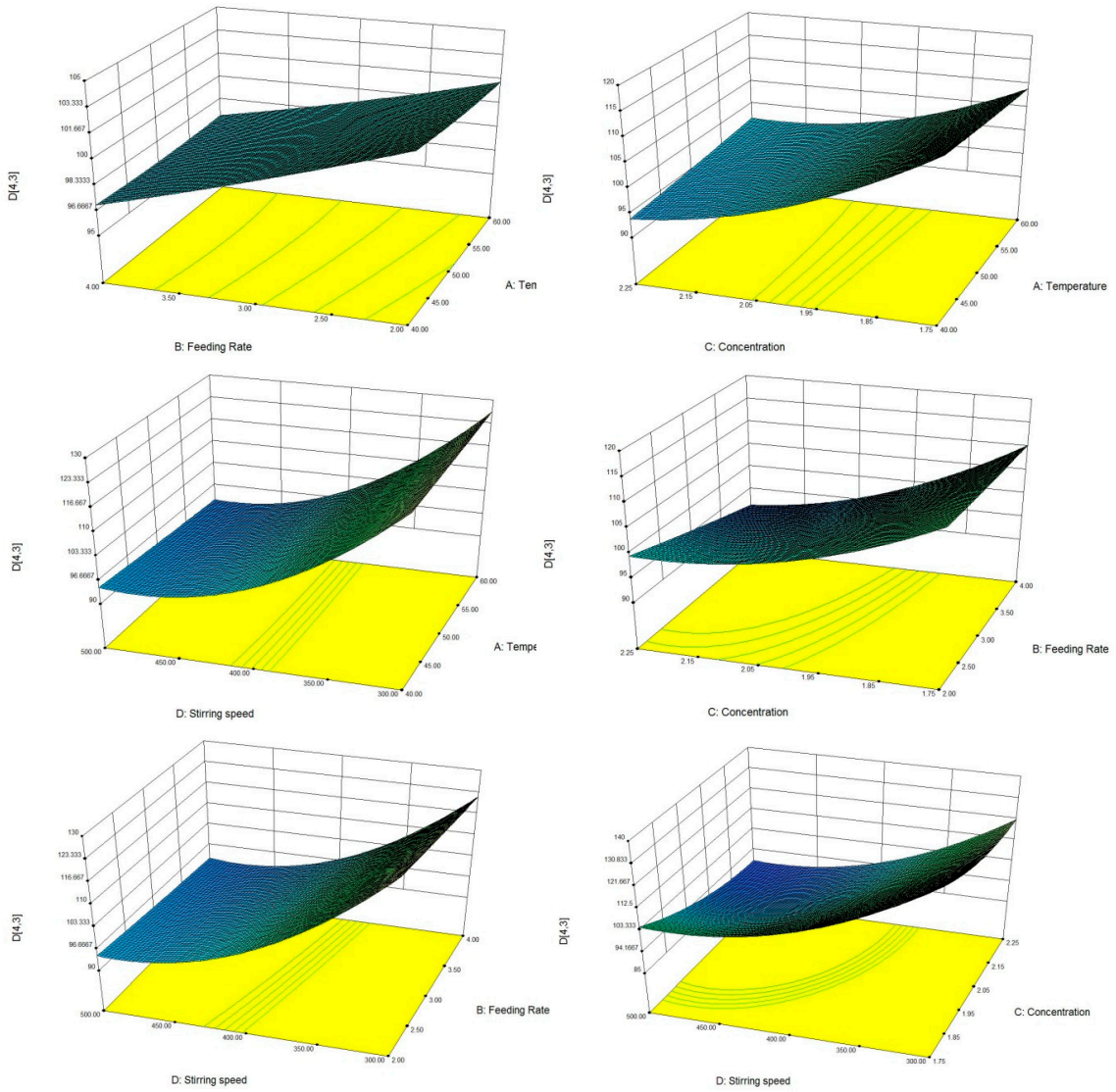

Figure 7. 3D surface plots of effects of binary interactions among factors A (temperature), B (feeding rate), C (concentration), and D (stirring speed) on response value Y_2 (particle size of Li_2CO_3).

4. Conclusions

The reactive crystallization kinetics and mechanism of the production of Li_2CO_3 from Li_2SO_4 and Na_2CO_3 solutions have been explored in this work on the basis of induction time measurements, and the complex crystallization process was modeled and optimized in regard to yield and particle size by response surface methodology. It was shown, expectedly, that the plotted $\log(t_{ind})$ versus $(\log S)^{-2}$ follows a linear relationship where there is a region of lower slope at lower supersaturation and a region of higher slope at higher supersaturation, thus indicating two distinct primary nucleation behaviors in which the heterogenous nucleation dominates at low supersaturations and at high supersaturations the homogenous nucleation governs. The transition point between heterogenous and homogenous nucleation was found to vary with temperatures but the nucleation order remained nearly the same under experimental conditions. Further, the growth mechanism of Li_2CO_3 reactive crystallization was determined to be 2D nucleation-mediated growth. Modeling of the reactive crystallization process of Li_2CO_3 was developed and process optimization was performed in regard to product yield and particle size. Response surface and ANOVA analysis revealed the major factors contributing to the yield and particle size of Li_2CO_3 crystallization were solution concentration and stirring speed, respectively. To the best of our knowledge, this work represents the first time that the nucleation and growth

mechanisms of reactive crystallization of Li_2CO_3 from Li_2SO_4 and Na_2CO_3 solutions and process modeling and optimization by response surface methodology have been studied. Our findings could be applied to the design and control of the reactive crystallization of Li_2CO_3 in its production from lithium sulfate sources.

Author Contributions: Conceptualization, S.Z., J.G. (Jie Gao) and W.T.; Methodology, S.Z. and Y.M.; Software, S.Z. and S.M.; Validation, Y.H., Y.M. and F.Z.; Formal Analysis, W.T., J.G. (Junbo Gong) and B.Z.; Investigation, S.Z. and J.G. (Jie Gao); Resources, J.G. (Jie Gao), C.L. and B.Z.; Data Curation, F.Z. and B.Z; Writing-Original Draft Preparation, S.Z. and J.G. (Jie Gao); Writing-Review & Editing, W.T.; Visualization, S.Z. and Y.H.; Supervision, J.G. (Junbo Gong) and W.T.; Project Administration, W.T., J.G. (Junbo Gong) and C.L.; Funding Acquisition, F.Z. and B.Z.

Funding: This research was funded by the China Postdoctoral Science Foundation, the open foundation of the State Key Laboratory of Chemical Engineering (no. SKL-ChE-18B04) and National Natural Science Foundation of China (nos. NNSFC 21808159 and 91634117).

Conflicts of Interest: The authors declare no competing financial interest.

References

1. Fergus, J.W. Recent Developments in Cathode Materials for Lithium Ion Batteries. *J. Power Sources* **2010**, *195*, 939. [CrossRef]
2. Garrett, D.E. Part 1—Lithium. In *Handbook of Lithium and Natural Calcium Chloride*; Elsevier: Amsterdam, The Netherlands, 2004.
3. Lazarus, J.H.; McGregor, A.M.; Ludgate, M.; Darke, C.; Creagh, F.M.; Kingswood, C.J. Effect of Lithium Carbonate Therapy on Thyroid Immune Status in Manic Depressive Patients: A Prospective Study. *J. Affect. Disord.* **1986**, *11*, 155. [CrossRef]
4. Bauer, D.; Diamond, D.; Li, J.; Sandalow, D.; Telleen, P.; Wanner, B. *Critical Materials Strategy*; U.S. Department of Energy: Washington, DC, USA, 2010.
5. Aguilar, P.G.; Graber, T.A. Determination of the Reaction Kinetic Parameters for Li_2CO_3 Crystallization from Li_2SO_4 and Na_2CO_3 Solutions Using Calorimetric Measurements. *Ind. Eng. Chem. Res.* **2018**, *57*, 4815–4823. [CrossRef]
6. An, J.W.; Kang, D.J.; Tran, K.T.; Kim, M.J.; Lim, T.; Tran, T. Recovery of Lithium from Uyuni Salar Brine. *Hydrometallurgy* **2012**, *117*, 64. [CrossRef]
7. Ogawa, Y.; Koibuchi, H.; Suto, K.; Inoue, C. Effects of the Chemical Compositions of Salars de Uyuni and Atacama Brines on Lithium Concentration during Evaporation. *Resour. Geol.* **2014**, *64*, 91. [CrossRef]
8. Choubey, P.K.; Kim, M.-S.; Srivastava, R.R.; Lee, J.-C.; Lee, J.-Y. Advance Review on the Exploitation of the Prominent Energy-Storage Element: Lithium. Part I: From Mineral and Brine Resources. *Miner. Eng.* **2016**, *89*, 119. [CrossRef]
9. Sun, Y.; Song, X.; Wang, J.; Luo, Y.; Yu, J. Unseeded Supersolubility of Lithium Carbonate: Experimental Measurement and Simulation with Mathematical Models. *J. Cryst. Growth* **2009**, *311*, 4714–4719. [CrossRef]
10. Sun, Y.; Song, X.; Wang, J.; Luo, Y.; Yu, J. Determination of seeded supersolubility of lithium carbonate using FBRM. *J. Cryst. Growth* **2010**, *312*, 294–300. [CrossRef]
11. Wang, H.Y.; Du, B.Q.; Wang, M. Study of the Solubility, Supersolubility and Metastable Zone Width of Li_2CO_3 in the LiCI-NaCI-KCI-Na_2SO_4 System from 293.15 to 353.15 K. *J. Chem. Eng. Data* **2018**, *63*, 1429–1434. [CrossRef]
12. Taborga, P.; Brito, I.; Graber, T.A. Effect of additives on size and shape of lithium carbonate crystals. *J. Cryst. Growth* **2017**, *460*, 5–12. [CrossRef]
13. Matsumoto, M.; Morita, Y.; Yoshinaga, M.; Hirose, S.; Onoe, K. Reactive Crystallization of Lithium Carbonate Nanoparticles by Microwave Irradiation of Aqueous Solution Containing CO_2 Microbubbles. *J. Chem. Eng. Jpn.* **2009**, *42*, S242–S248. [CrossRef]
14. Kuldipkumar, A.; Kwon, G.S.; Zhang, G.G.Z. Determining the growth mechanism of tolazamide by induction time measurement. *Cryst. Growth Des.* **2007**, *7*, 234–242. [CrossRef]
15. Sohnel, O.; Mullin, J.W. Interpretation of crystallization induction periods. *J. Colloid Interface Sci.* **1988**, *123*, 43–50. [CrossRef]

16. Van der Leeden, M.C.; Verdoes, D.; Kashchiev, D.; van Rosmalen, G.M. Induction time in seeded and unseeded precipitation. *Adv. Ind. Cryst.* **1991**, 31–46.
17. Montgomery, D.C. *Design and Analysis of Experiments*; John Wiley & Sons: New York, NY, USA, 2005.
18. Dutka, B.M.; Ditaranto, M.; Løvås, T. Application of a Central Composite Design for the Study of NOx Emission Performance of a Low NOx Burner. *Energies* **2015**, *8*, 3606–3627. [CrossRef]
19. Dutta, A.; Dowe, N.; Ibsen, K.N. An economic comparison of different fermentation configurations to convert corn stover to ethanol using Z. mobilis and Saccharomyces. *Biotechnol. Prog.* **2009**, *26*, 64–72.
20. Bas, D.; Boyaci, I.H. Modeling and optimization I: Usability of response surface methodology. *J. Food Eng.* **2007**, *78*, 836–845. [CrossRef]
21. Thorat, A.A.; Dalvi, S.V. Liquid antisolvent precipitation and stabilization of nanoparticles of poorly water soluble drugs inaqueous suspensions: Recent developments and future perspective. *Chem. Eng. J.* **2012**, *181*, 1–34. [CrossRef]
22. Gomez-Morales, J.; Torrent-Burgues, J.; Rodriguez-Clemente, R. Nucleation of calcium carbonate at different initial pH conditions. *J. Cryst. Growth* **1996**, *169*, 331–338. [CrossRef]
23. Mullin, J.W.; Ang, H.M. Nucleation characteristics of aqueous nickel ammonium-sulfate solutions. *Faraday Discuss.* **1976**, *61*, 141–148. [CrossRef]
24. Wojciechowski, K.; Kibalczyc, W. Light-scattering study of KH_2PO_4 and $BaSO_4$ nucleation process. *J. Cryst. Growth* **1986**, *76*, 379–382. [CrossRef]
25. Mersmann, A.; Kind, M. Chemical engineering aspects of precipitation from solution. *Chem. Eng. Technol.* **1988**, *11*, 264–276. [CrossRef]
26. Pastero, L.; Massaro, F.R.; Aquilano, D. Experimental and Theoretical Morphology of Single and Twinned Crystals of Li_2CO_3 (Zabuyelite). *Cryst. Growth Des.* **2007**, *7*, 2749–2755. [CrossRef]
27. Box, G.E.P.; Hunter, J.S.; Hunter, W.G. *Statistics for Experimenters: Design, Innovation, and Discovery*; Wiley-Interscience: Hoboken, NJ, USA, 2005; pp. 447–455.
28. Dahmoune, F.; Remini, H.; Dairi, S.; Aoun, O.; Moussi, K.; Bouaoudia-Madi, N.; Madani, K. Ultrasound assisted extraction of phenolic compounds from P. lentiscus L. leaves: Comparative study of artificial neural network (ANN) versus degree of experiment for prediction ability of phenolic compounds recovery. *Ind. Crop. Prod.* **2015**, *77*, 251–261. [CrossRef]